Thermal transients in a U-bend

Alex Skillen[a,*], Małgorzata J. Zimoń[b], Robert Sawko[b], Ryan Tunstall[c],
Charles Moulinec[a], David R Emerson[a]

[a]*STFC Daresbury Laboratory, Warrington WA4 4AD, UK*
[b]*IBM Research UK, Daresbury Laboratory, Warrington WA4 4AD, UK*
[c]*Rolls-Royce, Raynesway, Derby, DE21 7BE, UK*

Abstract

We study numerically the propagation of a hot thermal transient through a U-bend via an ensemble of wall-resolved large eddy simulations. Conjugate heat transfer between fluid and solid domains is accounted for. The flow is in a fully turbulent mixed convection regime, with a bulk Reynolds number of $10,000$, a Richardson number of 2.23, and water as the working fluid (Prandtl number $= 6$). These conditions lead to strong thermal stratification, with buoyancy-induced secondary flows, and the generation of a large and persistent recirculation region.

The evolution of Dean vortices as the thermal transient passes is studied. It is found that baroclinic vorticity generation dominates over a large period of the transient, due to the thermal inertia of the wall. Gravitational buoyancy leads to a reversal of the counter-rotating vortex pair. The impact of this reversal on the swirl-switching and secondary-current losses is assessed. It is found that low frequency modes are suppressed in the reversed-vortex state.

Keywords: Stratified flow, Baroclinic vorticity generation, Nuclear thermal-hydraulics, Statistically unsteady flow, Reversed secondary flow

---

*Corresponding author

1. Introduction

As a fluid flows around a bend, a local imbalance between the centripetal force and the opposing pressure gradient acts to transport low-inertia near-wall fluid towards the centre of curvature. This induces a counter-rotating vortex pair, known as Dean vortices, as fluid is subsequently transported back along the symmetry plane. The impact these Dean vortices have upon heat and mass transfer within the pipe is generally significant, and can be characterised by the dimensionless Dean number: $Dn \equiv Re\sqrt{D(2R_c)^{-1}}$ (where Re, D and R_c are the bulk Reynolds number, the pipe inner-diameter and radius of curvature, respectively).

A number of studies have systematically quantified the behaviour of flow around bends with circular cross section. Improvements in numerical modelling of developing laminar flows in U-shaped pipe were suggested by Humphrey at el. [1], enabling better understanding of the secondary fluid motions. In a turbulent setting, secondary flow development was investigated by Azzozal et al. [2] both experimentally (using a laser Doppler anemometer) and numerically. These studies were continued by Baughn et al. [3] focusing on local heat transfer measurements for similar turbulent configurations. Although the problem of flows in curved pipes has been extensively studied over the past several decades, there is still a relative lack in understanding in the flow physics, and particularly the instabilities involved.

At moderate to high Dean numbers, instabilities in the flow manifest as a cyclical change in the strength and size of the left and right Dean vortices relative to one another [4]. This phenomenon is known as swirl-switching. A number of computational [4, 5] and experimental [6, 7, 8] studies have investigated the physics of swirl-switching, and a review has been conducted by Vester et al. [9]. Transverse forces induced by swirl-switching can have significant impact upon the fatigue-life of plant components [10]. It is generally accepted the switching occurs as a gradual low-frequency shift between states, rather than an abrupt change from one bi-stable state to another [11].

A range of frequencies associated with swirl-switching have been reported. Although reported values vary (often significantly) between different studies, it is generally accepted the swirl-switching has both low and high frequency modes. For example, Hellström et al. [7] report two characteristic Strouhal numbers, St, of 0.16 and 0.33 ($St \equiv fDU^{-1}$, where U is the bulk velocity and f is the frequency). Recent work by Wang et al. [12] has highlighted that the recorded frequency of swirl-switching is highly sensitive to local flow properties, which may explain the discrepancies in recorded frequencies between different authors. Furthermore, their study highlights the role of large upstream structures on the low-frequency mode, while the higher-frequency mode originates from structures generated within the pipe-bend.

In the present study, we are concerned with the dynamics of flow in a U-bend as a hot thermal transient propagates throughout the domain. This case is relevant to the loop seal of a pressurised water nuclear fission reactor, amongst others. Both hot and cold thermal transients in a U-bend have been studied experimentally by Viollet [13] by applying a linear ramp to the inlet temperature over a short duration. Viollet observed that under the conditions of sufficiently low Reynolds number and Froude number, thermal stratification tends to occur. Stratification can significantly alter the flow, leading to the formation of a large buoyancy-induced recirculation region and steep temperature gradients. Furthermore, cyclical changes in inlet temperature, alternating between hot and cold states, can lead to thermal fatigue.

The impact of buoyancy upon Dean vortices has been investigated in a number of studies. Lingrani et al. [14] studied experimentally the effect Dean vortices have upon surface heat transfer in a curved channel. They were primarily interested in forced convection flows, but faced challenges in removing buoyancy effects from their experiments. Mixed convection Nusselt numbers were therefore measured, and a correlation was given to convert mixed convection Nusselt numbers into forced convections ones.

Ciofalo et al. [15] investigated computationally the influence of both gravitational and centrifugal buoyancy for laminar flow within a coiled pipe. They

performed a parameter study over a range of Richardson numbers with a linear increase in the pipe-wall temperature in the axial direction.

Kurnia et al. [16] performed calculations of laminar flow in straight and helical pipes of various cross section. They fixed the wall temperature and considered three different temperature differentials between wall and inlet. The dilatable working fluid (air) lead to conditions in which both gravitational and centrifugal buoyancy effects were significant. The study highlighted the formation of secondary vortices due to buoyancy in straight pipes, as well as the interaction between buoyancy-driven secondary flows and Dean vortices in the helical pipe cases.

In the aforementioned studies, [14, 15, 16], the temperature differential between the near-wall fluid and bulk-fluid was generated by heating (or cooling) the wall. To the best of our knowledge, the impact a *thermal transient* has upon Dean vortex dynamics and swirl-switching has not been previously studied. It is anticipated that a thermal transient, in conjunction with high wall thermal inertia, would lead to conditions in which large radial temperature (and density) gradients are present. In *mixed convection* flows, the gravitational and centrifugal buoyancy due to these density gradients has the potential to generate secondary flow, similar to those observed by Kurnia et al. [16]. The aim of this work is to test this hypothesis, and assess the impact a hot thermal transient has upon Dean vortex dynamics and swirl-switching within a U-bend configuration under turbulent mixed convection conditions.

This paper is structured as follows. In Section 2 we outline our methodology. In Section 3, key findings are presented. Finally, in Section 4 conclusions are drawn, and recommendations for future work are made.

2. Methodology

2.1. Governing Equations

We employ an operator splitting strategy to decompose the problem into fluid and solid domains. The fluid flow is governed by the incompressible fil-

tered Navier-Stokes equations (i.e. Large Eddy Simulations, (LES)) with the Boussinesq approximation to account for buoyancy (the impact of this approximation is to be discussed in Section 2.2), and a reduced filtered-energy equation to account for heat transfer:

$$\frac{\partial \overline{u}_i}{\partial x_i} = 0 \tag{1}$$

$$\frac{\partial \overline{u}_i}{\partial t} + \frac{\partial (\overline{u}_i \overline{u}_j)}{\partial x_j} = \frac{\partial}{\partial x_j} \left[-\frac{\overline{p}}{\rho_0} \delta_{ij} + \nu \left(\frac{\partial \overline{u}_i}{\partial x_j} + \frac{\partial \overline{u}_j}{\partial x_i} \right) - \tau_{ij} \right] - \rho_0 \beta \left(\overline{T} - T_0 \right) g_i \tag{2}$$

$$\frac{\partial \overline{T}}{\partial t} + \frac{\partial (\overline{u}_i \overline{T})}{\partial x_i} = \frac{\partial}{\partial x_j} \left(\alpha \frac{\partial \overline{T}}{\partial x_j} - q_j \right) \tag{3}$$

where an overbar denotes a filtered variable, and δ_{ij} is the Kronecker delta. The filtering operation is performed implicitly by the mesh. The field variables u, p and T denote the velocity, pressure and temperature, respectively, while t denotes the time. The constants are ρ_0 – the reference density, T_0 – the reference temperature, g – the gravitational acceleration, β – the thermal expansion coefficient, ν – the kinematic viscosity and α – the thermal diffusivity. Finally, τ_{ij} and q_j are the residual stress tensor and sub-grid heat flux, respectively.

The dynamic Smagorinsky eddy viscosity model provides turbulence closure [17, 18, 19]:

$$\tau_{ij} = -2c_s \Delta^2 \left| \overline{S} \right| \overline{S}_{ij}, \qquad q_j = \frac{(c_s \Delta^2 \left| \overline{S} \right|)}{Pr_t} \frac{\partial \overline{T}}{\partial x_j}. \tag{4}$$

where $\overline{S}_{ij}$ is the resolved strain-rate tensor, $\left| \overline{S} \right| \equiv \sqrt{2\overline{S}_{ij}\overline{S}_{ij}}$, Δ is the local filter width, Pr_t is the turbulent Prandtl number, and c_s is a model constant which is allowed to vary spatially and temporally; i.e. $c_s = c_s(\mathbf{x}, t)$. We dynamically set c_s according to the Germano-Lilly procedure [18, 19]. This dynamic sub-grid model was chosen since it is valid for relaminarised regions of the flow, as may be encountered in stably stratified turbulence.

In the solid domain, the transport of heat is accounted for via a reduced form of Equation 3 in which the convective and sub-grid terms are zero. The coupling between domains is achieved by enforcing consistency in both the temperature and heat flux at the interface:

$$T_s = T_f \tag{5}$$

$$\kappa_s \left.\frac{\partial \overline{T}}{\partial n}\right|_s = -\kappa_f \left.\frac{\partial \overline{T}}{\partial n}\right|_f \tag{6}$$

where subscripts $(\cdot)_f$ and $(\cdot)_s$ denote the fluid and solid domains, respectively, κ is the thermal conductivity, and n is the outward-pointing interface-normal.

The governing equations are discretised by the finite-volume method with Δ taken as $V^{1/3}$ (where V is the local cell volume), and are solved with the CFD package Code_Saturne (Version 5) [20].

2.2. Study Parameters

The fluid flow can be characterised by the Reynolds number (Re), gravitational Richardson number (Ri) and Prandtl number (Pr):

$$Re \equiv \frac{UD}{\nu}, \qquad Ri \equiv \frac{g\beta(T_1 - T_0)D}{U^2}, \qquad Pr \equiv \frac{\nu}{\kappa},$$

where U is the bulk velocity. In the present study, we set $Re = 10,000$, $Ri = 2.23$, and $Pr = 6$. These parameters lead to mixed convection flow conditions that are based on the study of [13], and relevant to the nuclear industry (amongst others).

Note that by employing the Boussinesq approximation to account for buoyancy (see Section 2.1), the centrifugal buoyancy is neglected. The impact of this approximation can be quantified through consideration of the centrifugal Richardson number:

$$Ri_c \equiv \frac{\beta(T_1 - T_0)D}{R_c}.$$

6

The ratio of Ri_c to Ri is then given by

$$\frac{Ri_c}{Ri} = \frac{U^2}{gR_c}.$$

From the definition of Re, this can be rewritten as:

$$\frac{Ri_c}{Ri} = \frac{(\nu Re)^2}{D^2 gR_c},$$

which for the present study is less than 9×10^{-4} if $D > 0.2$m. Similarly, the temperature-induced density difference is less than 0.5% if $D > 0.2$m, and hence the Bousinessq approximation is reasonable for sufficiently large D.

The final dimensionless groups dictating the rate of conductive heat flow between fluid and solid domains are the ratio of thermal diffusivities, α_s/α_f, and the ratio of thermal conductivities, κ_s/κ_f. In the present study, we employ a ratio of $\alpha_s/\alpha_f = 144.8$, and $\kappa_s/\kappa_f = 123.5$, which is representative of water flowing within a steel pipe. This is different to the experiments of [13], where altu-glass pipework was employed, and hence the thermal boundary condition was closer to adiabatic.

2.3. Geometry and Mesh

A schematic of the geometry is given in Figure 1. The vertical inlet and outlet sections are $10D$ in length, while the near-horizontal section is $6D$ in length with a 1% downward slope. This slope is a feature of the Viollet case [13], and is an approximation of the pipework downstream of the steam-generator outlet of the Superphénix reactor.

The radius of curvature, R_c, for both bends is $1.5D$, while the wall-thickness is $0.05D$. All walls are smooth. This geometry is based on that of [13], but has a longer vertical inlet section. The reason for this change is to allow development of the inflow synthetic turbulence prior to the region of interest, as will be discussed in Section 2.4.

7

The data presented herein has been computed on a block-structured mesh comprising approximately $47M$ hexahedral cells ($43M$ and $4M$ for the fluid and solid domains, respectively). The near-wall grid spacing was such that $y^+ < 0.2$ was maintained throughout the domain (with a corresponding $T^+ < 1.2$) and hence no additional near-wall modelling or damping terms were required (note the use of a dynamic sub-grid model, which precludes the need for near-wall damping).

A mesh sensitivity study has been conducted with a mesh comprising approximately $24M$ cells. We observed no appreciable difference in low-order statistics (mean velocity and temperature fields). The ensemble size (see Section 2.5 for details) for the coarse mesh (ten runs) was insufficient for converged higher-order statistics, hence the sensitivity of higher-order terms to the mesh cannot be ruled out.

2.4. Initial and Boundary Conditions

At the interface between fluid and solid domains, the no-slip condition provides a boundary condition for the velocity, while a zero-gradient Neumann condition is applied for the pressure. Unless otherwise stated, the interface temperature is set via the conjugate transfer of heat between the domains, as described in Section 2.1. At the external wall of the pipe, a zero gradient Neumann condition was applied for the temperature. Additional runs with an adiabatic wall thermal boundary condition have also been performed for comparison purposes.

Correlated inflow data, with prescribed first- and second-order statistics was generated via the Synthetic Eddy Method (SEM) [21, 22]. The statistical input to the SEM was generated via a precursor Reynolds Averaged Navier-Stokes (RANS) simulation of fully-developed pipe-flow, also at $Re = 10,000$, in which the Elliptic Blending Reynolds Stress Model (EBRSM) [23] provided turbulence closure. Note that we deliberately do not account for the change in the mean velocity profile and Reynolds stress tensor at the inlet due to upstream thermal stratification. Our aim is to assist reproducibility, and hence a simple station-

ary condition for the velocity and Reynolds stresses was favoured. Moreover, tests showed that the synthetic turbulence reached a mature state within $\sim 2D$ (assessed via the development of wall skin-friction coefficient) – well before the first bend. This development length is in line with previous work at a similar Reynolds number [22].

The flow was initialised by conducting an isothermal LES computation at reference temperature T_0. The solution was time-marched to a statistically-steady state, to provide initial conditions to the main computation. At time $\tilde{t}(\equiv Ut/D) = 0$, we initiated the thermal transient by linearly increasing the inlet temperature to a value T_1. This linear ramp acts until $\tilde{t} = 7.5$. For all times $\tilde{t} > 7.5$, the inlet temperature remains fixed at T_1. The magnitude of the temperature difference, $(T_1 - T_0)$, is dictated by the Richardson number, Ri.

At the outlet, zero-gradient Neumann conditions were applied for all variables, with the exception of the pressure which had a Dirichlet condition applied.

2.5. Statistical Data

Due to the transient nature of the flow, averaging is conducted via an ensemble. We generate a total of forty realisations of the flow, each by seeding the random number generator of the synthetic inflow method differently. This was done at the start of the isothermal initialisation computation. This ensemble size is sufficient for well-converged low-order statistics, and reasonable convergence of higher-order statistics (enough to be useful in the assessment of unsteady-RANS models, for example). The convergence of the ensemble is assessed via Table 1.

3. Results and Discussion

3.1. Flow and Heat Transfer Overview

In Figure 2, ensemble averaged streamlines showing the temporal evolution of the flow are presented. The formation of a large buoyancy-induced recirculation region is observed, qualitatively matching the observations of [13]. It can be

9

seen that the thermal stratification persists for several dimensionless time-units, indicating limited heat transfer into the recirculation region.

Figure 3 shows contours of the fluid-solid interface temperature evolution. At times $\tilde{t} = 30$ and $\tilde{t} = 45$, the dominant feature of the plots is the stratification-induced cold wall region along the bottom of the near-horizontal section. Also noteworthy is the temperature lag of the wall. This is caused by the wall's significant thermal inertia. For instance, by $\tilde{t} = 15$ the thermal transient has propagated beyond the first bend (the thermal-front is located within the near-horizontal section). Yet the interface temperature at $z/D \gtrsim 9$ is still at (or very close to) T_0. For the vertical pipe section, at $z/D < 10$ the interface temperature is significantly below T_1 even by $\tilde{t} = 30$, and has still not reached the final temperature by $\tilde{t} = 45$. Clearly this interface temperature is not correctly captured with an adiabatic wall boundary condition (where the thermal inertia is zero). The role this thermal inertia has upon the flow-physics will become apparent in the following discussion.

In Figure 4, we present contours of the fluid-solid interface Nusselt number evolution. Interestingly, negative Nusselt number regions are observed towards the end of the transient. This indicates that one mode of heat transfer into the cold recirculation region is via the solid domain; as the upper portion of the near-horizontal pipe wall heats up, heat is transferred circumferentially through the solid domain by conduction. Below the cold recirculation region, some of this heat is subsequently transferred back to the fluid from below, leading to a negative Nusselt number.

Wall shear-stress vectors are shown in Figure 5. At all times, a small recirculation region is observed on the inner radius of each bend (apparent by negative streamwise skin-friction). It is interesting to note that for time $\tilde{t} = 30$, the reversed flow after the second bend continues all the way to the exit of the domain (note the negative streamwise skin-friction at $\theta \approx \pi$, and $z > 20$). This is due to rapid flow acceleration as the thermal transient reaches the downstream vertical section and experiences unstable stratification. This generates a buoyant plume, and rapid flow acceleration. Fluid entrainment by this plume

leads to a recirculation region, in accordance with mass conservation. This is in qualitative agreement with the observations of [13].

It can be seen from Figure 5, at time $\tilde{t} = 0$ there is a secondary transport (by the Dean vortices) from $\theta = 0$ towards $\theta = \pi$ after each bend. The centripetal force associated with the pipe bend causes low-inertia near-wall fluid to be transported towards the centre of curvature (at $\theta = \pi$). Interestingly, by $\tilde{t} = 15$, the secondary transport is in the opposite direction to that which would be expected from Dean vortices. To investigate this further, we plot vectors of the secondary flow at a section $1D$ downstream of the end of the first bend (see Figure 6). At time $\tilde{t} = 0$, classical Dean vortices are observed. At $\tilde{t} = 15$ the secondary flow is suppressed, and starting to reverse. By $\tilde{t} = 30$, a strong counter-rotating vortex pair is observed, with opposite sign to that at time $\tilde{t} = 0$. This can be explained by consideration of the thermal inertia of the wall, and the buoyancy-driven secondary flow this induces. As the hot-front enters into the near-horizontal section of the pipe, the fluid at the core of the pipe is hotter and lighter than the cold near-wall fluid (cold, due to the large thermal-inertia of the wall). Buoyancy-driven density currents are initiated, which dominate the centripetal force. The cold near-wall fluid sinks, generating a pair of counter-rotating vortices with opposite sign to that of the Dean vortices. This is qualitatively similar to the results of Kurnia et al. [16], with the exception that their density gradient was induced by fixing the wall temperature, while ours is due to the combination of a thermal transient and the wall's thermal inertia.

By $\tilde{t} \approx 70$, we observe a second reversal in the secondary flow as the wall heats up, and the centripetal force again dominates. This is apparent in the final frame of Figure 6, where two pairs of counter-rotating vortices can be seen; one due to the centripetal force as the Dean vortices re-establish, and the other (smaller) pair due to buoyancy induced by the thermal inertia of the wall. Eventually, we would expect only Dean vortices, identical to time $\tilde{t} = 0$, as the flow becomes isothermal again at temperature T_1. The computations were not run to the new isothermal state.

11

To confirm that the reversal of the secondary flow is indeed due to the thermal inertia of the wall, we have also conducted an ensemble of adiabatic runs. All details of the adiabatic computations are identical to those of the conjugate heat transfer runs (mesh, ensemble size, etc.) with the exception of the thermal boundary condition on the inner wall. In Figure 7, the secondary flow at time $\tilde{t} = 30$ is compared for the two different thermal boundary conditions. It can be seen that in the adiabatic case, the secondary flow is in the opposite direction to that of the conjugate heat transfer case, thus confirming the thermal inertia of the wall does indeed reverse the sign of the secondary vortices. This highlights the importance of including the solid domain for transient computations of mixed or natural convection, where the thermal inertia of the wall is high .

Profiles of the ensemble-averaged temperature on the symmetry plane, at $\tilde{t} = 30$, are shown in Figure 8. From this figure, the extent of the stratification region is apparent. The impact an adiabatic boundary condition has is also apparent from this figure. Significant differences in the thermal field are apparent between the conjugate and adiabatic cases, highlighting the major influence this secondary flow has upon the global heat transfer characteristics of the pipework. Again, this highlights the importance of including the solid domain. The remainder of this paper focuses on the conjugate heat transfer results.

3.2. Vorticity Budgets

We study the budgets of the vorticity transport equation in order to elucidate further the mechanism of secondary-flow reversal. The vorticity transport equation can be obtained by applying the curl operator to the momentum transport equation, and is written as

$$\underbrace{\frac{D\omega_i}{Dt}}_{\mathcal{I}} = \underbrace{\omega_j \frac{\partial u_i}{\partial x_j}}_{\mathcal{II}} + \underbrace{\epsilon_{ijk} \frac{1}{\rho_0} \frac{\partial(\beta T)}{\partial x_j} \frac{\partial p}{\partial x_k}}_{\mathcal{III}} + \underbrace{\nu \frac{\partial^2 \omega_i}{\partial x_j \partial x_j}}_{\mathcal{IV}}, \tag{7}$$

where ϵ_{ijk} is the Levi-Civita symbol. On the right hand side, $\mathcal{II}$ is the vortex stretching term, $\mathcal{III}$ is the baroclinic torque, and $\mathcal{IV}$ is the viscous diffusion of

12

vorticity. The baroclinic term is active when the density gradient is misaligned with the pressure gradient. In our case, at the exit of the first bend, the pressure gradient balances the centrifugal and hydrostatic forces, and hence has a large vertical component. Meanwhile, the density gradient acts in approximately the wall-normal direction, due to the thermal inertia of the wall. At $\theta = \pi/2$, we would thus expect the baroclinic term to be large as the transient passes, but before the wall has fully heated. In Figure 9, we plot the vorticity budgets in the wall-normal direction at $\theta = \pi/2$. It can be seen that the baroclinic term, $\mathcal{III}$, is the dominant source of vorticity production as the thermal transient passes. This vorticity is redistributed by viscous diffusion ($\mathcal{IV}$) which balances the baroclinic production term. Note that the residual of Equation (7) is not zero, as is apparent from studying Figure 9. This is due to the lack of convergence of the higher-order terms (the convective term in $\mathcal{I}$, and the vortex stretching term, $\mathcal{II}$) due to the sample size available for ensemble averaging. Despite this, it is apparent that the baroclinic term (which is well converged) is the dominant mode of vorticity production for times where the thermal transient is present.

3.3. Swirl-Switching

Swirl-switching can affect the fatigue life of pipes where the flow is subjected to a bend. We are interested in assessing how the thermal transient affects this phenomenon. Swirl-switching can be characterised through the swirl number, Sw, which is defined as the ratio of the flux of angular momentum in the axial direction and the flux of axial momentum in the axial direction, normalised by pipe radius:

$$Sw = \frac{\int r\rho U_\theta U_{ax} dA}{D/2 \int \rho |U_{ax}| U_{ax} dA},$$ (8)

where U_θ and U_{ax} are the tangential and axial velocity components, respectively. Figure 10 shows the temporal evolution of Sw integrated over a plane $1D$ downstream of the first bend. It is apparent from the plot that the amplitude of the swirl number decreases between $\tilde{t} \approx 12 - 20$. This is when the thermal transient

13

reaches the plane under consideration, and the secondary-flow starts to change direction.

In order to assess the frequency of the swirl-switching, we perform a continuous wavelet transform (CWT) to the $Sw(\tilde{t})$ signal, using a Morlet mother wavelet [24]. This allows us to transform the time signal to the frequency domain, and is applicable to a non-stationary signal. To reduce the noise in the spectral power estimation, we ensemble average the CWT coefficients over an ensemble size of three runs (note the smaller ensemble size than for the flow statistics, due to the availability of data). This process is analogous to Welch's method for spectral density estimation for a stationary signal. The resulting scalogram is presented in Figure 11. It can be seen from the figure that prior to the arrival of the thermal transient ($\tilde{t} \lesssim 10$) there are two dominant frequencies at $St \equiv fD/U \approx 0.1$ and $St \approx 0.3$. This is in agreement with prior studies of the flow in pipe bends [7]. As the secondary flow reversal progresses ($12 \lesssim \tilde{t} \lesssim 20$), the spectral power is significantly reduced over a broadband range of frequencies. Indeed, there are no statistically significant peaks in the spectral power estimation. As the reversed state of secondary flow establishes itself (at $\tilde{t} \gtrsim 20$), there appears to be only one dominant frequency at $St \approx 0.3$. The low frequency mode that was present for $\tilde{t} \lesssim 10$ has been suppressed. Since this low frequency mode is thought to originate from the large-scale structures upstream of the bend [12], one possible explanation for this observation is the turbulence-suppressing effects of stable stratification, which reduce the kinetic energy contained within the large structures.

Figures 12 and 13 show contours of the normalised axial velocity $0.05D$ from the wall, for times $\tilde{t} = 0$ and $\tilde{t} = 30$, respectively. Also presented in the plots is a reconstruction using the first five POD modes, in order to highlight the most energetic structures. From Figure 12, long streak-like structures are clearly visible, typical of wall-bounded turbulence. Comparing this with Figure 13, it is apparent that the long structures are indeed significantly less pronounced due to the stable stratification, potentially explaining the lack of the low-frequency mode in the swirl-switching as the thermal transient passes.

14

4. Conclusion

In this paper, we studied the flow through a U-bend that is subject to a thermal transient. An interesting feature is the reversal of the secondary flow due to buoyancy. The thermal inertia of the wall causes the near-wall fluid to sink, opposing the motion due to Dean vortices, leading to a reversal of the secondary flow. Misalignment of the pressure gradient and density gradient generates a baroclinic torque, which is the dominant production term in the vorticity transport equation.

The impact of the secondary flow reversal on swirl-switching has been assessed. It was found that the swirl number has a diminished amplitude for a period while the reversal is establishing. Subsequent to this, there appears to be a single dominant frequency for the reversed state, contrary to the isothermal case in which there are two dominant frequencies (a low frequency mode, superimposed upon a high-frequency mode). A physical explanation for this has been proposed: the stable stratification due to the thermal transient leads to lower levels of turbulent fluctuations in the upstream vertical pipe. Low-frequency modes due to the large scale structures originating upstream of the bend are therefore less pronounced.

In the near-horizontal section of the pipe, we observe strong flow stratification, and a large recirculation region over a portion of the transient. The impact of the secondary-flow reversal on the heat and mass transfer within the near-horizontal section is significant. One mode of heat transfer into the stratification region is by the reversed secondary flow. This highlights the importance of including the solid domain in this calculation; without accounting for the thermal inertia of the wall, the secondary flow would be driven by the centripetal force. Another mode of heat transfer into the stratification region is via conduction through the solid pipe wall. Again, this could not be accounted for without including the solid domain. We have also performed this computation with an adiabatic thermal boundary condition, in order to quantify the impact neglecting the solid domain has. Significant differences in temperature profiles

15

between the conjugate and adiabatic cases have been observed.

Although we have looked at flow in a U-bend, buoyancy-driven secondary flow should be expected to occur in any mixed convection flows where the thermal inertia of the wall is large, and a thermal transient of sufficient magnitude propagates through the domain, including in straight pipes or ducts. A useful extension to this work may be to experimentally observe this reversal of the secondary flow under a broad parameter space.

Supplementary material

Full 3D volumetric datasets containing ensemble averaged data can be downloaded from [25].

Acknowledgements

References

References

[1] J. Humphrey, H. Iacovides, B. Launder, Some numerical experiments on developing laminar flow in circular-sectioned bends, Journal of Fluid Mechanics 154 (1985) 357–375.

[2] J. Azzola, J. Humphrey, H. Iacovides, B. Launder, Developing turbulent flow in a u-bend of circular cross-section: measurement and computation, Journal of fluids engineering 108 (2) (1986) 214–221.

[3] J. Baughn, H. Iacovides, D. Jackson, B. Launder, Local heat transfer measurements in turbulent flow around a 180-deg pipe bend, Journal of Heat transfer 109 (1) (1987) 43–48.

[4] C. Carlsson, E. Alenius, L. Fuchs, Swirl switching in turbulent flow through 90 pipe bends, Physics of Fluids 27 (8) (2015) 085112.

[5] F. Rütten, W. Schröder, M. Meinke, Large-eddy simulation of low frequency oscillations of the dean vortices in turbulent pipe bend flows, Physics of Fluids 17 (3) (2005) 035107.

[6] J. Sakakibara, N. Machida, Measurement of turbulent flow upstream and downstream of a circular pipe bend, Physics of fluids 24 (4) (2012) 041702.

[7] L. H. Hellström, M. B. Zlatinov, G. Cao, A. J. Smits, Turbulent pipe flow downstream of a 90° bend, Journal of Fluid Mechanics 735.

[8] A. Kalpakli, R. Örlü, Turbulent pipe flow downstream a 90° pipe bend with and without superimposed swirl, International Journal of Heat and Fluid Flow 41 (2013) 103–111.

[9] A. K. Vester, R. Örlü, P. H. Alfredsson, Pod analysis of the turbulent flow downstream a mild and sharp bend, Experiments in Fluids 56 (3) (2015) 57.

[10] R. Tunstall, D. Laurence, R. Prosser, A. Skillen, Large eddy simulation of a t-junction with upstream elbow: The role of dean vortices in thermal fatigue, Applied Thermal Engineering 107 (2016) 672–680.

[11] R. Röhrig, S. Jakirlić, C. Tropea, Comparative computational study of turbulent flow in a 90 pipe elbow, International Journal of Heat and Fluid Flow 55 (2015) 120–131.

[12] Z. Wang, R. Örlü, P. Schlatter, Y. M. Chung, Direct numerical simulation of a turbulent 90 bend pipe flow, International Journal of Heat and Fluid Flow 73 (2018) 199–208.

[13] P. Viollet, Observation and numerical modelling of density currents resulting from thermal transients in a non rectilinear pipe, Journal of Hydraulic Research 25 (2) (1987) 235–261.

[14] P. Ligrani, S. Choi, A. Schallert, P. Skogerboe, Effects of dean vortex pairs on surface heat transfer in curved channel flow, International Journal of Heat and Mass Transfer 39 (1) (1996) 27–37.

[15] M. Ciofalo, A. Arini, M. Di Liberto, On the influence of gravitational and centrifugal buoyancy on laminar flow and heat transfer in curved pipes and coils, International Journal of Heat and Mass Transfer 82 (2015) 123–134.

[16] J. C. Kurnia, A. P. Sasmito, T. Shamim, A. S. Mujumdar, Numerical investigation of heat transfer and entropy generation of laminar flow in helical tubes with various cross sections, Applied Thermal Engineering 102 (2016) 849–860.

[17] J. Smagorinsky, General circulation experiments with the primitive equations: I. the basic experiment, Monthly weather review 91 (3) (1963) 99–164.

[18] M. Germano, U. Piomelli, P. Moin, W. H. Cabot, A dynamic subgrid-scale eddy viscosity model, Physics of Fluids A: Fluid Dynamics 3 (7) (1991) 1760–1765.

[19] D. K. Lilly, A proposed modification of the germano subgrid-scale closure method, Physics of Fluids A: Fluid Dynamics 4 (3) (1992) 633–635.

[20] Y. Fournier, J. Bonelle, C. Moulinec, Z. Shang, A. Sunderland, J. Uribe, Optimizing code_saturne computations on petascale systems, Computers & Fluids 45 (1) (2011) 103–108.

[21] N. Jarrin, S. Benhamadouche, D. Laurence, R. Prosser, A synthetic-eddy-method for generating inflow conditions for large-eddy simulations, International Journal of Heat and Fluid Flow 27 (4) (2006) 585–593.

[22] A. Skillen, A. Revell, T. Craft, Accuracy and efficiency improvements in synthetic eddy methods., International Journal of Heat and Fluid Flow 62 (2016) 386–394.

[23] R. Manceau, K. Hanjalić, Elliptic blending model: A new near-wall reynolds-stress turbulence closure, Physics of Fluids 14 (2) (2002) 744–754.

[24] S. Mallat, A wavelet tour of signal processing, Elsevier, 1999.

[25] A. Skillen, 3D datasets for "Thermal transients in a U-Bend" (2019). `doi: 10.5286/edata/732`.

Nomenclature

D	Pipe inner diameter.
Dn	Dean number.
f	Frequency.
g	Acceleration due to gravity.
R_c	Bend radius of curvature.
Ri	Gravitational Richardson number.
Ri_c	Centrifugal Richardson number.
Re	Reynolds number.
p	Pressure.
Pr	Prandtl number.
Pr_t	Turbulent Prandtl number.
Sw	Swirl number.
T	Temperature.
T_0	Reference (initial) temperature.
T_1	Final temperature.
t	Time.
$\tilde{t}$	Dimensionless time.
u	Velocity vector.
U	Bulk velocity.
$\mathbf{x}$	Position vector.
α	Thermal diffusivity.
β	Thermal expansion coefficient.
δ_{ij}	Kronecker delta.
Δ	Filter width.
ϵ_{ijk}	Levi-Civita symbol.
η	Wall-normal direction.
θ	Angle in cylindrical coordinate system.
κ	thermal conductivity.

ν	Kinematic viscosity.
ρ	Density.
ρ_0	Reference density.
ω	Vorticity vector.

Ensemble Size (runs)	$< T >_{RMS}$	$< u'u' >_{RMS}$
10	0.831	0.0519
20	0.830	0.0548
30	0.830	0.0557
40	0.830	0.0559

Table 1: Table showing convergence of root-mean-squared (RMS) $< T >$ and $< u'u' >$ for different ensemble sizes. RMS values were integrated over the symmetry plane.

Figures and tables (to be inserted at typesetting stage)
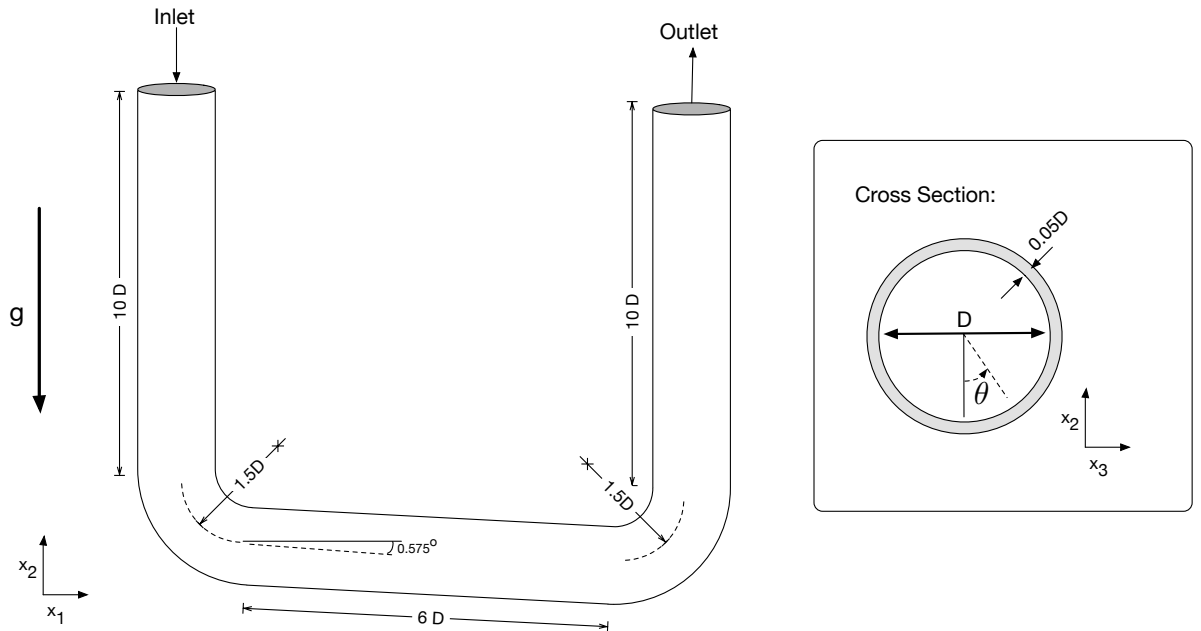
Figure 1: Schematic of the geometry
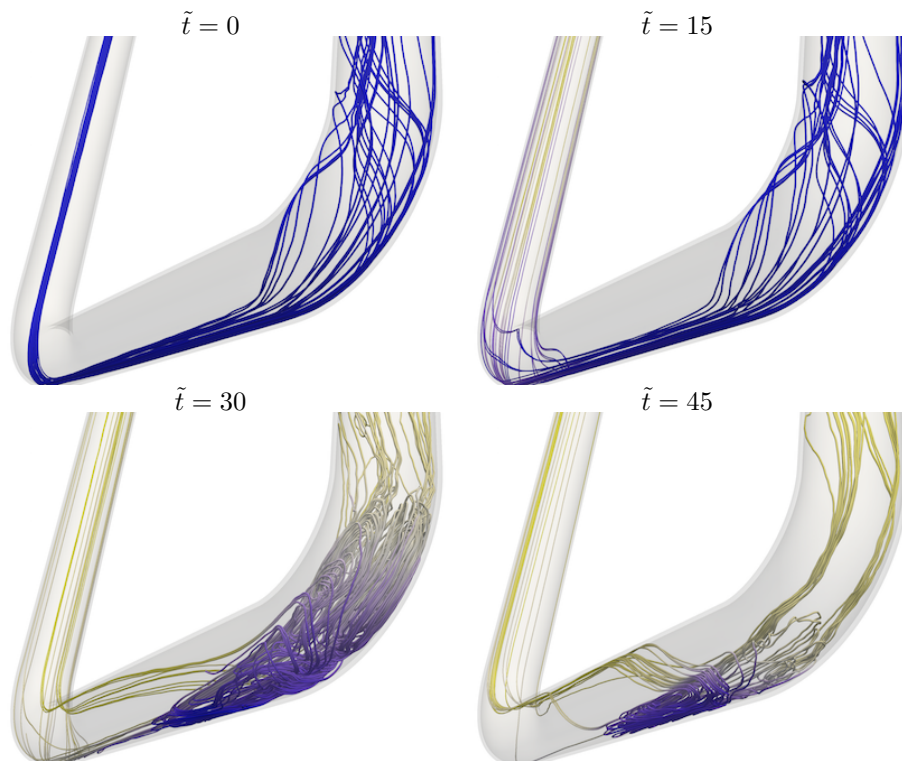
Figure 2: (Colour online) Ensemble averaged flow streamlines, coloured by temperature. All time-frames have their streamlines seeded at the same location. T_0: Blue. T_1: Yellow.
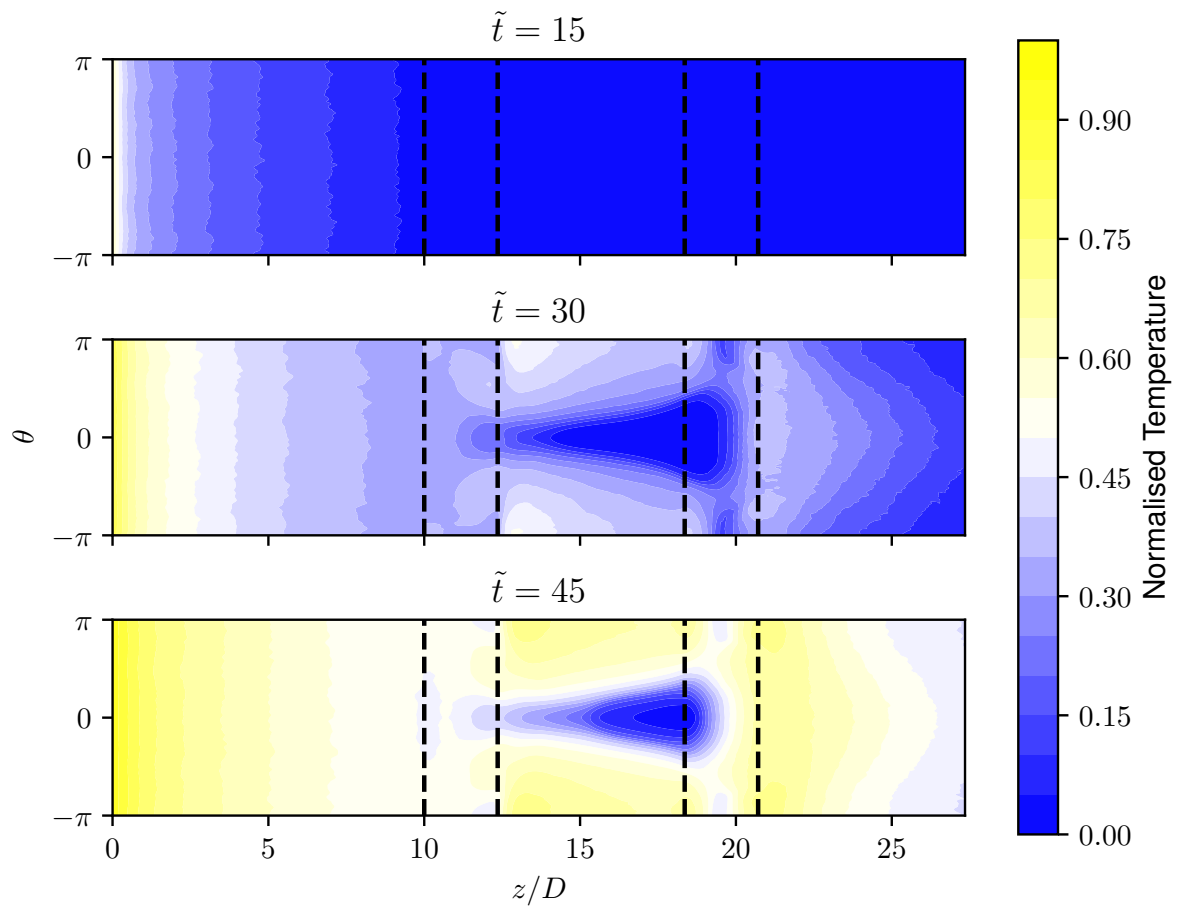
Figure 3: (Colour online) Flattened interface temperature contours (cylindrical coordinate system). Dashed lines denote locations of the two bends. The inlet is at $z/D = 0$.
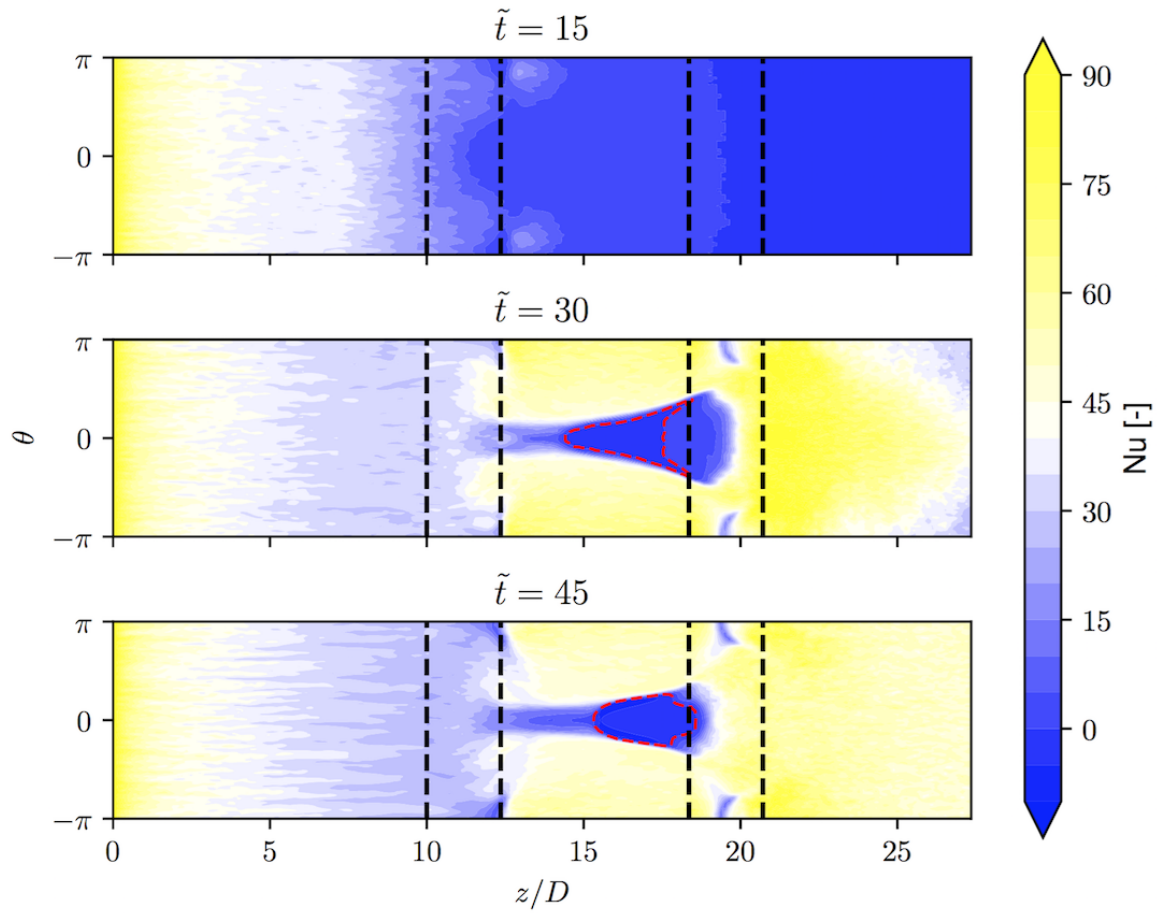
Figure 4: (Colour online) Flattened interface Nusselt number contours (cylindrical coordinate system). Zero contour highlighted by red-dashed line. Black dashed lines denote locations of the two bends. The inlet is at $z/D = 0$.
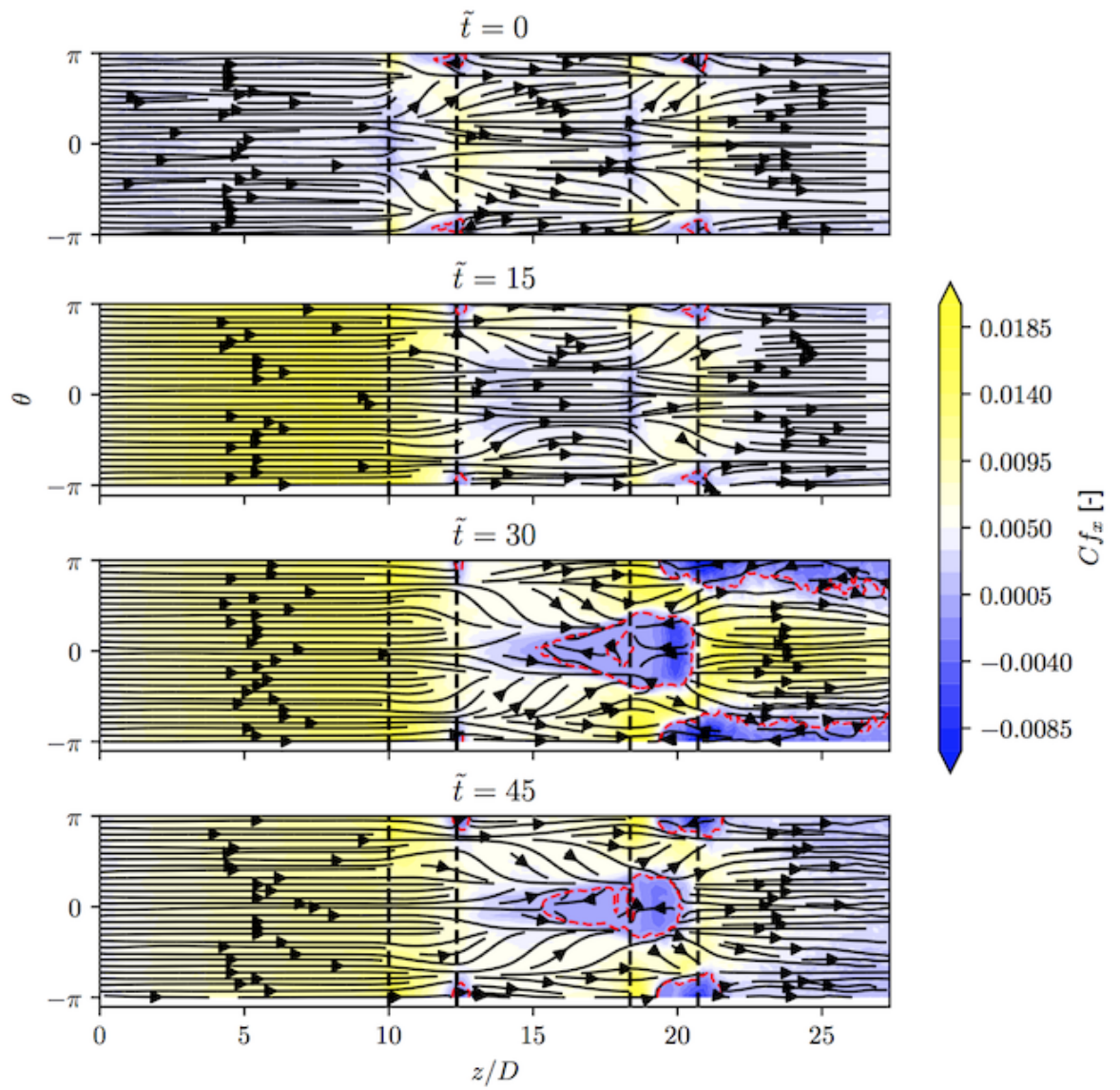
Figure 5: (Colour online) Interface skin-friction lines coloured by streamwise skin-friction component. The zero-contours of streamwise skin-friction are highlighted by the red-dashed lines. Dashed black lines denote locations of the two bends. The inlet is at $z/D = 0$.

26
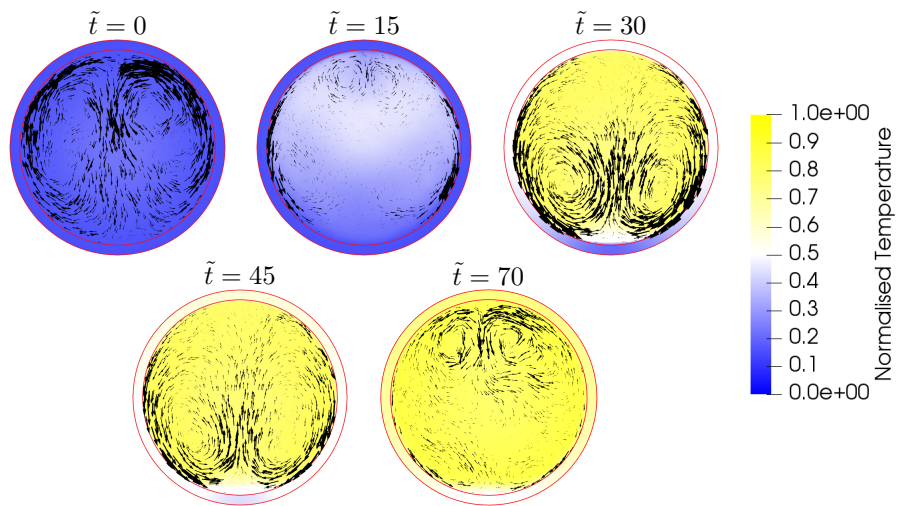
Figure 6: (Colour online) Ensemble averaged secondary flow, $1D$ downstream of the first bend, coloured by normalised temperature. Red outline denotes the boundaries of the solid domain.
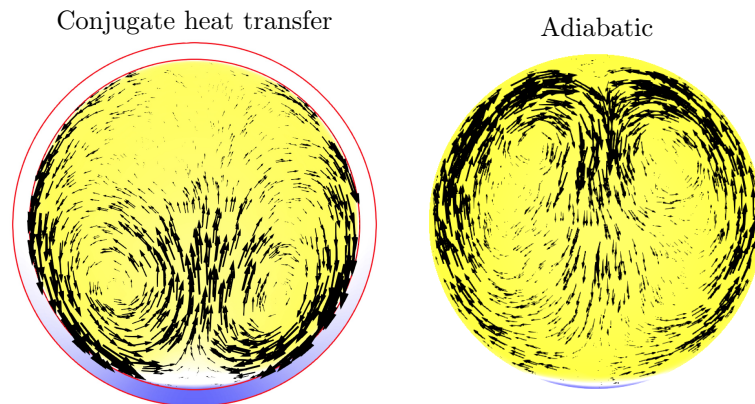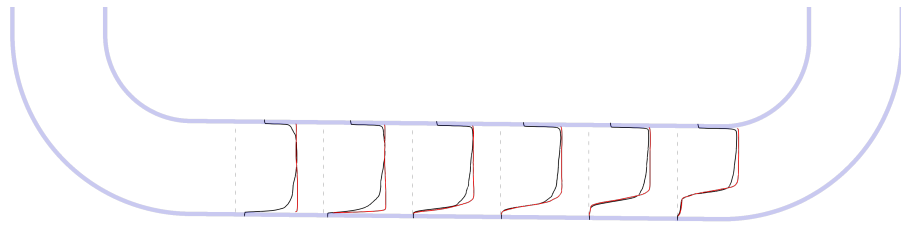

Figure 7: (Colour online) Ensemble averaged secondary flow at $\tilde{t} = 30$, $1D$ downstream of the first bend, coloured by normalised temperature (colour bar as in Fig. 6). Red outline denotes the boundaries of the solid domain.

Figure 8: (Colour online) Profiles of the ensemble averaged temperature on the symmetry plane, at $\tilde{t} = 30$ (Conjugate heat transfer – Black lines. Adiabatic boundary condition – red lines.). The profiles are taken at $x/D = 2$ to 7 in increments of 1, with the locations denoted by the dashed lines lines.
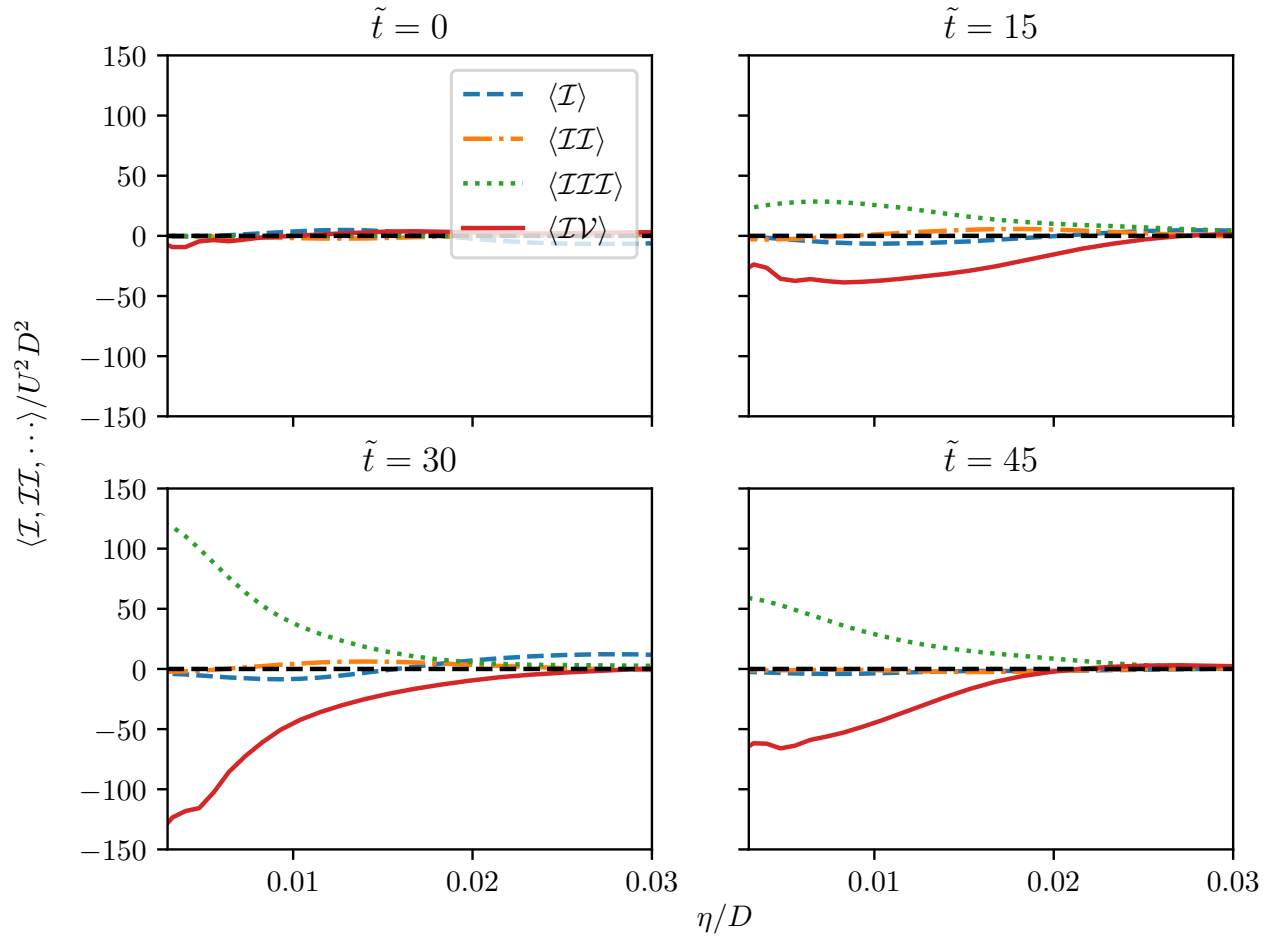
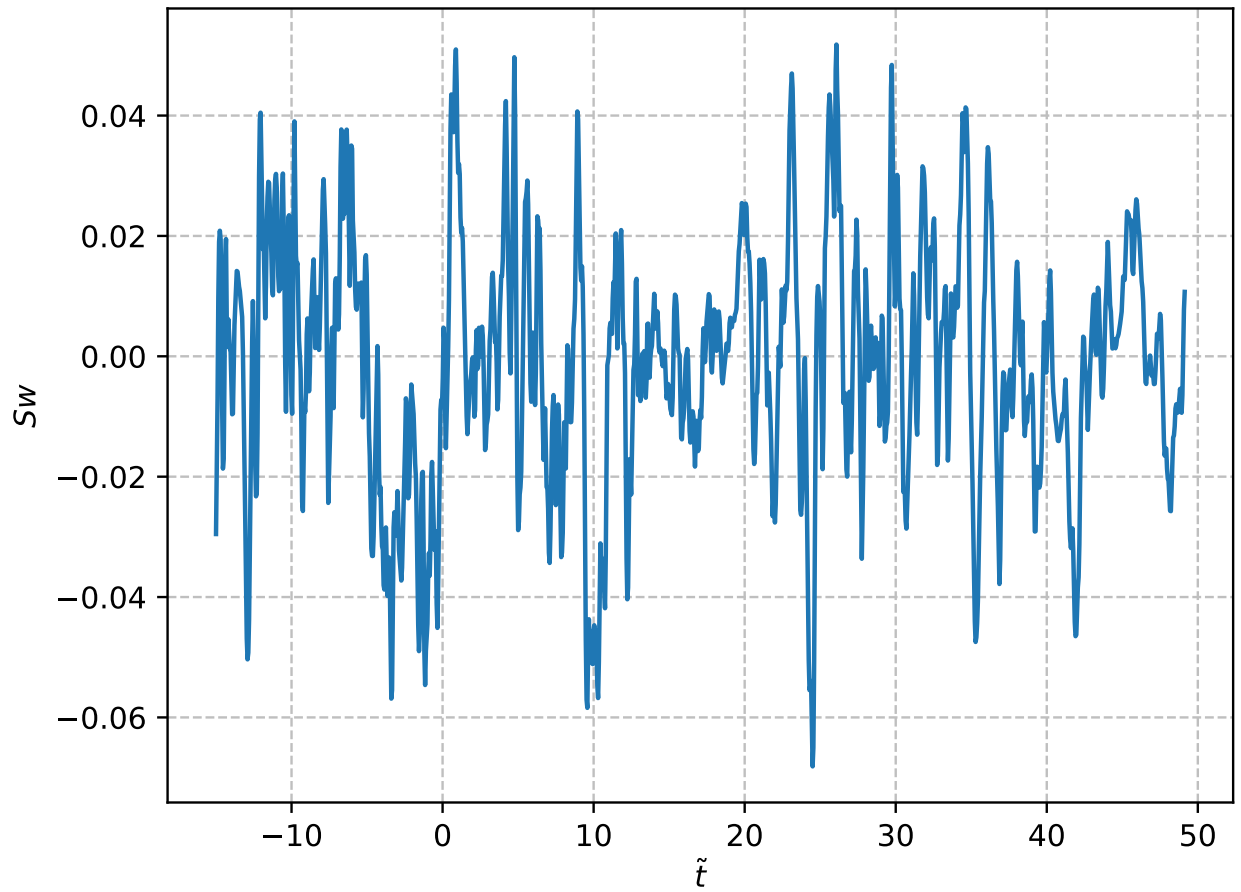Figure 9: (Colour online) Ensemble averaged streamwise vorticity budgets, $1D$ downstream of the first bend. Profiles are in the wall-normal direction (η), at $\theta = \pi/2$.

Figure 10: Evolution of the swirl-number, Sw, with time. Swirl number is integrated at the cross-section $1D$ downstream of the first elbow. Negative values of $\tilde{t}$ correspond to the isothermal flow, prior to the transient
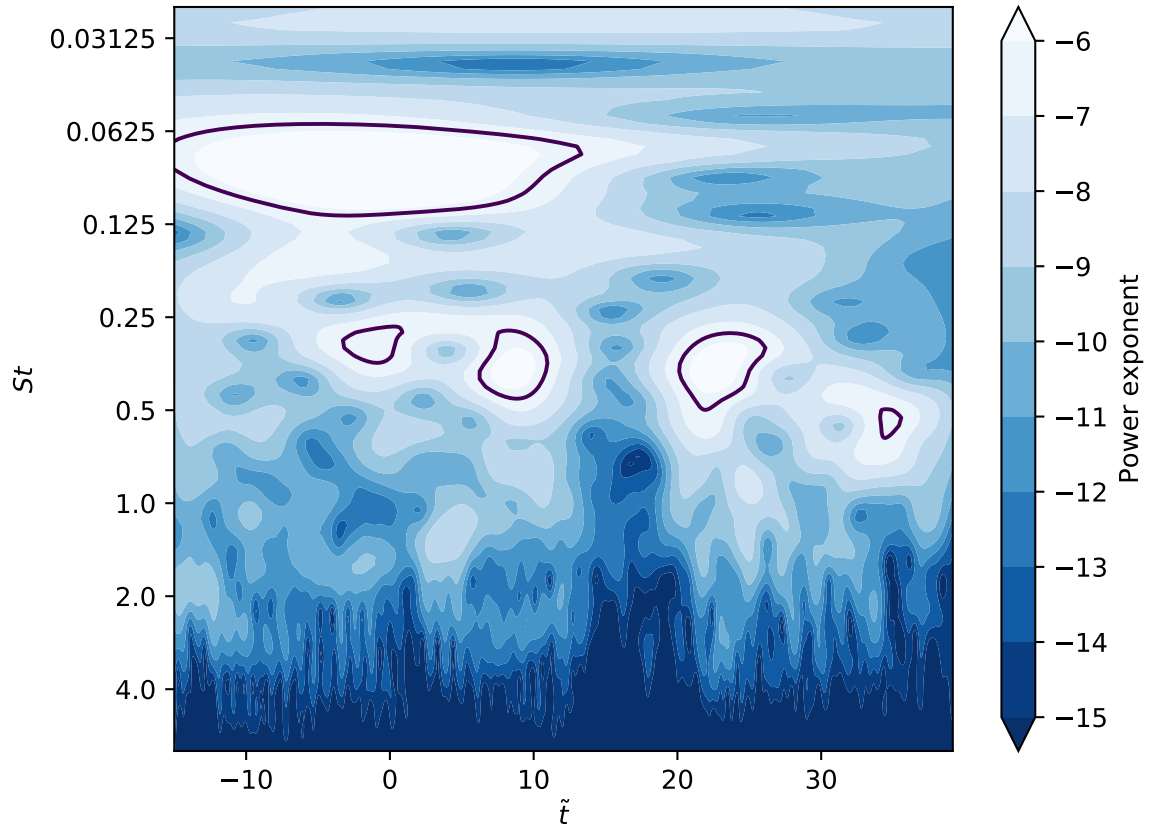
Figure 11: (Color online) Continuous wavelet transform scalogram showing the evolution of Strouhal number, (St), based upon the swirl number, (Sw). Swirl number is integrated at the cross-section $1D$ downstream of the first elbow. Black contour lines show statistically significant spectral peaks, with a 95% significance level.
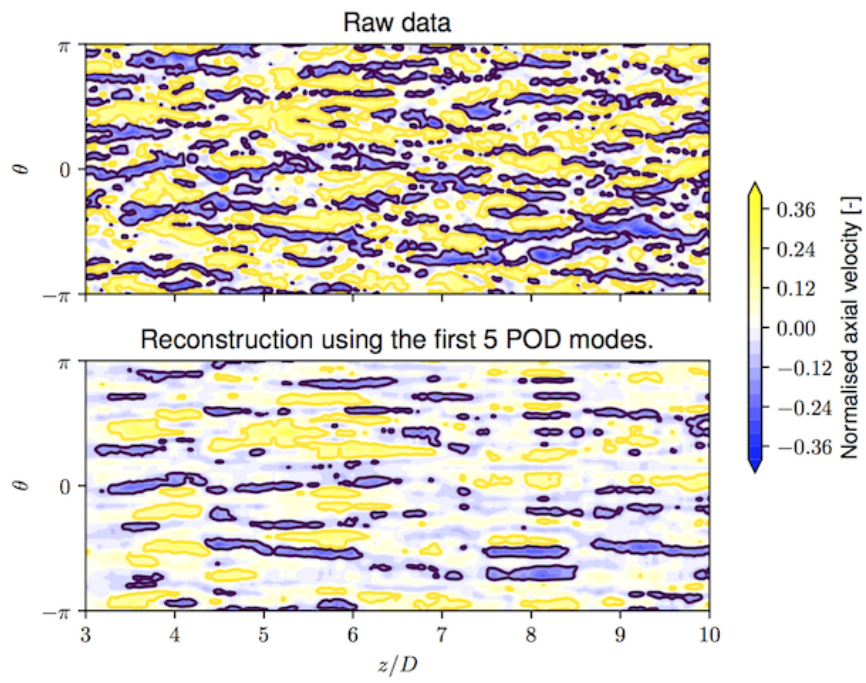
Figure 12: (Color online) Top: Contours of U_{ax}/U at time $\tilde{t} = 0$, taken $0.05D$ from the pipe wall. Bottom: A reconstruction using the first five POD modes, highlighting the most energetic structures. In both plots, the ± 0.1 contours are emphasised by darkened contour lines.
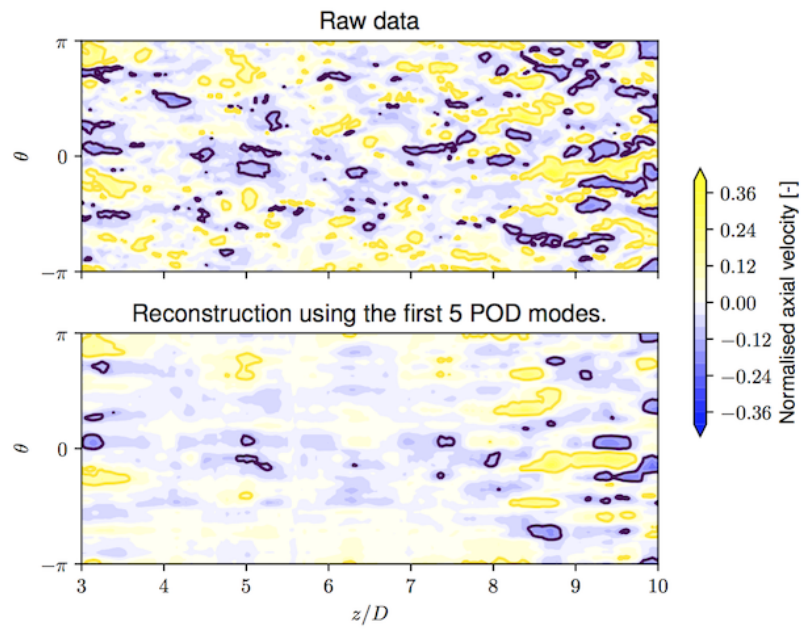
Figure 13: (Color online) Top: Contours of U_{ax}/U at time $\tilde{t} = 30$, taken $0.05D$ from the pipe wall. Bottom: A reconstruction using the first five POD modes, highlighting the most energetic structures. In both plots, the ± 0.1 contours are emphasised.